Cathodic stripping square-wave voltammetry for assessing As(III) removal with synthetic mixed oxides

Angélica C. Heredia, Jenny Gómez Avila, Fernando Garay & Mónica E. Crivello

Journal of Solid State Electrochemistry
Current Research and Development in Science and Technology

ISSN 1432-8488
Volume 21
Number 12

J Solid State Electrochem (2017)
21:3619-3629
DOI 10.1007/s10008-017-3709-x

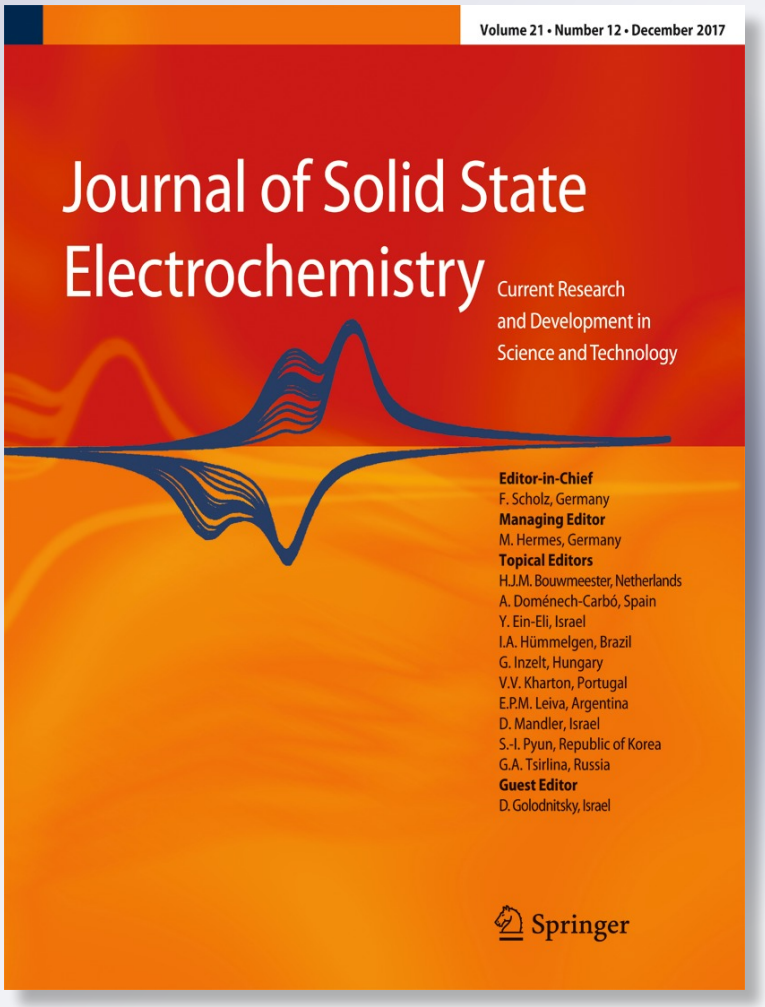

Springer

J Solid State Electrochem (2017) 21:3619–3629
DOI 10.1007/s10008-017-3709-x

ORIGINAL PAPER

Cathodic stripping square-wave voltammetry for assessing As(III) removal with synthetic mixed oxides

Angélica C. Heredia[1] · **Jenny Gómez Avila**[1] · **Fernando Garay**[2] · **Mónica E. Crivello**[1]

Received: 1 May 2017 / Revised: 20 July 2017 / Accepted: 23 July 2017 / Published online: 29 July 2017

Abstract In this work, the adsorption of As(III) species from aqueous solutions onto mixed oxides (MOs) synthesized from layered double hydroxides (LDHs) has been assessed by cathodic stripping square-wave voltammetry (CS-SWV). The optimized electrochemical protocol involves the accumulation of arsenic for 60 s at −0.4 V, in presence of 0.5 mM Cu(II), 0.3 μM pyrrolidine dithiocarbamate (PDTC), and 0.9 M HCl, followed by a reductive scan to −1.0 V. A stable and well-defined peak was observed at −0.780 V, with a linear range that goes from 2 to 110 μg L^{-1} of As(III). A value of limit of detection (LOD) = 4 μg L^{-1} was calculated as three times the ratio between the standard deviation of the ordinate and slope of the linear regression curve. The presence of Cu(II) increases the signal of current and minimizes the effect of interfering species, while PDTC forms a complex that stabilizes the signal observed during the cathodic scan. Ternary LDHs and their MOs composed by MgAlFe were synthesized and characterized as potential filtering materials. X-ray photoelectron spectroscopy and UV-Vis diffuse reflectance analysis showed that the Fe(III) ions can be found in tetrahedral and octahedral coordination environments, while SEM micrographs evidenced the cluster formation and aggregates of particles when the Fe/(Fe+Al) molar ratio is increased. The capacity of MOs for removing As(III) has been studied at different contact times in a batch reactor, and in all cases, removals of As(III) above 75% were achieved.

Keywords Electroanalysis · Mixed oxides · Layered double hydroxides · Square-wave voltammetry · Arsenic

Introduction

Water sources with high levels of oxyanions, such as arsenite, chromate, nitrite, and selenite among others, are considered toxic for humans and other living organisms [1–10]. This is because several of these compounds can bioaccumulate and favor the development of different types of diseases by prolonged exposure to high doses [9–12]. In the case of arsenic, there is evidence that the presence of high levels of As in drinking water causes bladder cancer and other skin diseases, including skin cancer [1–4, 9, 13]. Although there are some pesticides that contain arsenic, the presence of this element in water sources is usually associated with natural events [4, 13]. In 2006, the World Health Organization lowered the maximum allowable concentration of arsenic in drinking water to 10 μg L^{-1}. This regulation was soon followed by the US EPA bringing an urgent need for the development of arsenic sensors and the improvement of systems for water treatment [4, 9, 14]. In this context, there is still high interest for finding low-cost and human health friendly materials with high capacity for the removal of arsenic from aqueous solutions [1–3, 9, 14]. The major As-affected aquifers are encountered in semi-urban and rural areas of Argentina, Chile, Mexico, China, Hungary, Bangladesh, India, and Vietnam [4, 13]. Conventional bewildering techniques are difficult to practice in areas without centralized drinking water supply systems. Thus, simple, low-cost, and small-scale water treatment options are highly required to decontaminate water in those regions [4, 9].

✉ Angélica C. Heredia
angelicacheredia@gmail.com

[1] CITeQ-CONICET, Universidad Tecnológica Nacional, Facultad Regional Córdoba, Maestro Marcelo López esq. Cruz Roja Argentina, Ciudad Universitaria, X5016ZAA Córdoba, Argentina

[2] INFIQC-CONICET, Departamento de Físico Química, Facultad de Ciencias Químicas, Universidad Nacional de Córdoba. Pabellón Argentina, Ciudad Universitaria, X5000HUA Córdoba, Argentina

The removal of As in conventional treatment plants consists of the following steps: oxidation, coagulation-flocculation, filtration, and post-chlorination [14]. Filtering materials, such as Fe-Al binary oxide [15], zero valent iron [16], clay minerals (kaolinite, montmorillionite, and illite) [17], hydrous iron(III) oxide [18], and magnetite [19], have been used for removing As from contaminated water sources. Other processes such as inverse osmosis, electrodialysis, and nanofiltration have shown more efficiency for As removal than conventional treatments [20]. However, they usually involve relatively high levels of water rejection and are not necessarily competitive with respect to costs of conventional treatment systems [14].

In the last years, a class of anionic clays known as layered double hydroxides (LDHs) or hydrotalcite-like compounds has attracted substantial attention for industrial applications as well as for academic studies [21]. The synthesis of those materials is relatively simple and inexpensive since it consists of brucite layers where Mg(II) is replaced by triple-charged cations such as Al(III). The extra charge is compensated by anions that can be stored in the interlaminar region. The calcination of these LDH results on mixed oxides (MOs) characterized by large surface areas and high thermal stability. Those MOs have a property denominated the memory effect, which consists of recovering their original LDH structure when they are exposed to an aqueous solution or humid atmosphere. These properties, together with the good exchange capacity of LDHs, make them very promising materials for developing filter devices.

Although there are well-established spectroscopies that can be used for the analysis of arsenic, the labor and cost associated with those methods make electrochemical techniques the most promising approach [2, 8, 22–29]. In this regard, stripping voltammetric strategies have proven to give reliable results in laboratory conditions and provide a relatively low-cost option for the systematic analysis of samples coming from a batch reactor [8, 26–29]. To achieve detection limits of trace elements, arsenic species are usually reduced by a chemical reaction to As(III) and then accumulated at the electrode as As(0). Following the deposition step, the electrode potential is scanned to strip the accumulated As(0) from the electrode [1, 2, 8, 25]. Excess of Cu(II) is commonly added to avoid interferences related to the formation of intermetallic complexes of arsenic with traces of selenium and copper [30]. Under these conditions, the processes that take place at a SMDE can be described by the following equations [30]:

$$\text{Accumulation step}: \mathrm{As(III)} + 3/2\mathrm{Hg(Cu)} + 3\mathrm{e}^- \rightarrow 1/2\ \mathrm{Cu_3As_2} \quad (1)$$

$$\text{Stripping step}: 1/2\mathrm{Cu_3As_2} + 3\mathrm{H}^+ + \mathrm{Hg} + 3\mathrm{e}^- \rightarrow \mathrm{Cu(Hg)} + \mathrm{AsH_3} \quad (2)$$

Actually, Eqs. (1) and (2) provide a simple description of the reactions that are taking place during each step since the stoichiometry of intermetallic compounds of between Cu, Hg, and As depends on experimental conditions such as the nature and concentration of the supporting electrolyte, Cu(II) concentration, and accumulation potential [30]. Also, the addition of organic ligands with one or more thiol groups has shown to stabilize the voltammetric response of arsenic during cathodic and anodic scans. Linear swept voltammetry and differential pulse voltammetry have been used for the stripping scan of arsenic in presence of cysteine, pyrrolidine dithiocarbamate (PDTC), or diethyl dithiocarbamate on HMDE [31–33].

In this work, MOs of MgAlFe are synthesized from LDHs. These materials are characterized by different techniques and then applied for As removal. A protocol based on cathodic stripping square-wave voltammetry (CS-SWV) has been optimized for assessing the amount of As removed.

Experimental

All solutions were prepared with ultrapure water (18 M Ω cm) from a Millipore Milli-Q system (DI water). Analytical grade reagents HCl (Baker, Argentina), NaOH (Baker, Argentina), the others $CuCl_2{\cdot}2H_2O$, ammonium PDTC, $Mg(NO_3)_2$, $Al(NO_3)_3$, and $Fe(NO_3)_3$ are from Sigma-Aldrich, Argentina, and were used as received. A 0.0100 M As(III) stock solution was prepared from As_2O_3 (purity 99.99%, Sigma-Aldrich, Argentina). The stock solution was acidified with HCl to pH 2 and stored at 4 °C in a dark glass bottle to prevent oxidation of As(III). Standard solutions were prepared freshly from the stock solution at the beginning of a set of experiments.

Synthesis of MOs

LDH precursors containing different amounts of Mg, Al, and Fe were prepared by coprecipitation using the low supersaturation method at constant pH = (10.0 ± 0.5). In all cases, a constant molar ratio $[M^{2+}]/[M^{3+}] = 3$ was used, where $[M^{2+}]$ corresponds to the amount of Mg^{2+} and $[M^{3+}]$ to the total amount of Al^{3+} plus Fe^{3+}; the composition of each mixture is indicated in Table 1. Coprecipitation was performed by mixing two solutions. Solution A corresponds to a set of mixtures of $Mg(NO_3)_2$, $Al(NO_3)_3$, and $Fe(NO_3)_3$, each of them, dissolved in DI water. The total amount of cations $[M^{2+} + M^{3+}] = 0.7$, while the $[M^{3+}] = 0.17$ M. Solution B contains 0.085 M of Na_2CO_3. Both solutions were added simultaneously to 30 mL of DI water at a drip rate of 60 mL h^{-1}. The pH was kept constant by adding small amounts of NaOH 2 M. The resulting gel was aged for 18 h. Then it was washed with DI water and centrifuged at 2000 rpm until observing a

Table 1 Chemical composition and SSA of analyzed samples

Sample	$\frac{Mg^{2+}}{Al^{3+}+Fe^{3+}}$		$Fe^{3+} = \frac{Fe^{3+}}{Al^{3+}+Fe^{3+}} \times 100\%$		Specific surface area ($m^2\ g^{-1}$)		Total pore volume ($cm^3\ g^{-1}$)
	Theoretical	ICP	Theoretical	ICP	Precursor	Oxide	Oxide
HT_0	3	2.56	0	0	150	272	1.15
HT_{25}	3	2.75	25	24.3	129	212	0.90
HT_{50}	3	2.65	50	50.6	100	194	0.71
HT_{75}	3	1.59	75	73.1	91	110	0.59
HT_{100}	3	1.76	100	100	86	99	0.53

pH value equal to 7. The solid was dried overnight at 90 °C and finally calcined for 9 h at 450 °C in air atmosphere. The molar percentage of iron, $[Fe^{3+}]/([Al^{3+}] + [Fe^{3+}]) \times 100$, was changed from 0 to 100 and the samples have been denominated as HT_0, HT_{25}, HT_{50}, HT_{75}, and HT_{100}. The names of calcined samples are preceded with the letter C and the names of samples that were exposed to solutions with arsenic are preceded by As.

Characterization of MOs

Inductively coupled plasma (ICP) optical emission spectroscopy was used for the determination of the metal content in the oxides. The measurements were performed with a Varian Spectra AA 220 (Varian, USA).

The XRD powder patterns were collected on an X'pert diffractometer (PANanalytical, Netherlands) at a scan speed of 2/3 min in 2θ. The diffraction patterns were identified by comparison with those included in the software package PCPDFWIN from the International Centre for Diffraction Data (ICDD).

The spectra of UV-Vis diffuse reflectance (DRUV-Vis) were recorded using a Jasco V-650 spectrometer in the wavelength range of 200–1000 nm. Also, a Spectralon was used as reflectance standard.

X-ray photoelectron spectroscopy (XPS) analyses were carried out using an ESCA spectrometer (VG microtech, USA) with a non-monochromatic Mg K_α radiation (υ = 1253.6 eV) as the excitation source. High-resolution spectra were recorded in the constant pass energy mode at 20 eV, using a 720-mm diameter analysis area. Under these conditions, the Au $4f_{7/2}$ line was recorded with 1.16 eV full width at half maximum (FWHM) with a binding energy (BE) of 84.0 eV. The spectrometer energy scale was calibrated using Cu $2p_{3/2}$, Ag $3d_{5/2}$, and Au $4f_{7/2}$ photoelectron lines at 932.7, 368.3, and 84.0 eV, respectively. Charge referencing was done against adventitious carbon (C 1s, 284.8 eV). The pressure in the analysis chamber was maintained lower than 10^{-9} Torr. PHI ACCESS ESCA-V6.0 F software package was used for acquisition and data analysis. A Shirley-type background was subtracted from the signals.

The specific surface area (SSA) was determined by the Brunauer-Emmett-Teller (BET) method, which was recorded with an ASAP 2000 instrument (Micromeritics, USA). In order to eliminate the water physically adsorbed LDHs were degassed at 200 °C and the MOs at 390 °C; in both cases, the process was performed for 60 min. Total pore volume (TPV) was determined from N_2 adsorption-desorption isotherms obtained at the temperature of liquid nitrogen using a ASAP 2420 instrument (Micromeritics, USA). The images of scanning electron microscopy (SEM) were obtained with an accelerating voltage of 20 kV using a JSM-6380 LV (JEOL, Japan) and a Supra 40 (Carl Zeiss, Germany).

Batch adsorption experiments

The arsenic removal test was carried out in a batch reactor where 0.1 g of MOs was put in contact with 70 mL of 165 μg L^{-1} As(III) solution. The experiment was performed at 25 °C and the solution was stirred with a magnetic stirrer for 10 min. Once the removal test was finished, the solid fraction of MOs exposed to arsenic (As-MOs) was filtered through a Whatman filter paper no. 1 and then dried in nitrogen atmosphere at 90 °C. The resulting dried samples were analyzed by XRD to evaluate the structure of the samples As-MOs, while the soluble fraction was evaluated by CS-SWV to assess the remaining amount of As(III).

Electrochemical detection

Measurements were performed with an Autolab (Eco-Chemie, Utrecht, Netherlands), equipped with a PSTAT 30 potentiostat and the GPES 4.3 software package. A static mercury drop (VA 663 Metrohm, Switzerland) with a surface area of 0.40 mm^2 was used as the working electrode. A glassy carbon rod was the counter electrode and all potentials in the text are referred to a $Ag_{(s)}|AgCl_{(s)}|KCl_{(aq)}$ (3 M) reference electrode.

After extruding a new mercury drop, a pre-concentration step was applied under stirred conditions at the accumulation

potential (E_A) for t_A = 20 s. The potential was scanned in the negative direction, after a stabilization time of 5 s. The solution was degassed with high-purity nitrogen for 10 min prior to the measurements and for an additional 20 s before each scan. A nitrogen atmosphere was maintained throughout the experiments. Parameters in CS-SWV experiments were defined as usual and reducing current is considered to be negative [8, 10].

Results and discussion

X-ray diffraction

Figure 1 shows powder X-ray diffraction patterns of samples before and after calcination. LDH precursors with different iron content are shown in Fig. 1a. Some general features of HDLs are the sharp and intense lines observed at low values of 2θ and less intense and asymmetric lines observed for the rather high values of 2θ. The peaks located at 2θ of 11.62°, 23.38°, 34.43°, 60.5°, and 61.8° are related to the diffraction planes (003), (006), (009), (110), and (113), respectively [34]. All those planes are characteristic planes of hydrotalcite-like phases. According to the data of ICDD, most of the peak positions matched with the hydrotalcite phase (PCPDFWIN 70–2151) [34]. Since Mg^{2+}, Al^{3+}, and Fe^{3+} randomly occupy the octahedral holes of OH^- ions in a close-packed configuration, the signals assigned to planes (003) and (006) are used to calculate the basal spacing (d) between the brucite-like sheets. This distance is important because the excess of positive charge that is generated from the substitution of Mg^{2+} by Al^{3+} or Fe^{3+} can be compensated by carbonate anions or eventually by species of arsenic that lie between the brucite-like sheets. Another characteristic signal corresponds to the plane (110), which is employed to calculate the unit cell dimension (a), where $a = 2d_{110}$. The sample HT_0 presents sharp and well-defined peaks, whereas broader and less intense signals are observed according to the increment of iron content in the samples. In this regard, the increment of the amount of iron would diminish the crystallinity of the samples.

After calcination at 450 °C, the reflection planes (003) and (006) disappear due to the rupture of the laminar structure of all samples. Figure 1b shows the phases of the oxides obtained after calcination. The alumina Al_2O_3 phase does not show a diffraction pattern because it has amorphous structure when the calcination temperature is below 800 °C [35]. All patterns showed the presence of MgO in periclase phase (PCPDFWIN 78-0430) [34]. The XRD patterns also show that the ion Fe^{3+} crystallizes in two structures, spinel $MgFe_2O_4$ (PCPDFWIN 71-1232) and hematite Fe_2O_3 (PCPDFWIN 79-1741) [34]. Although the increment of iron content diminishes the crystallinity and the amount of MgO in periclase phase, it increases the amount of hematite and spinel phases associated with the peak that appears at 35.64° [34].

DRUV-Vis spectroscopy

The spectra DRUV-Vis of samples before and after calcination are shown in Fig. 2. The spectra have been deconvoluted into

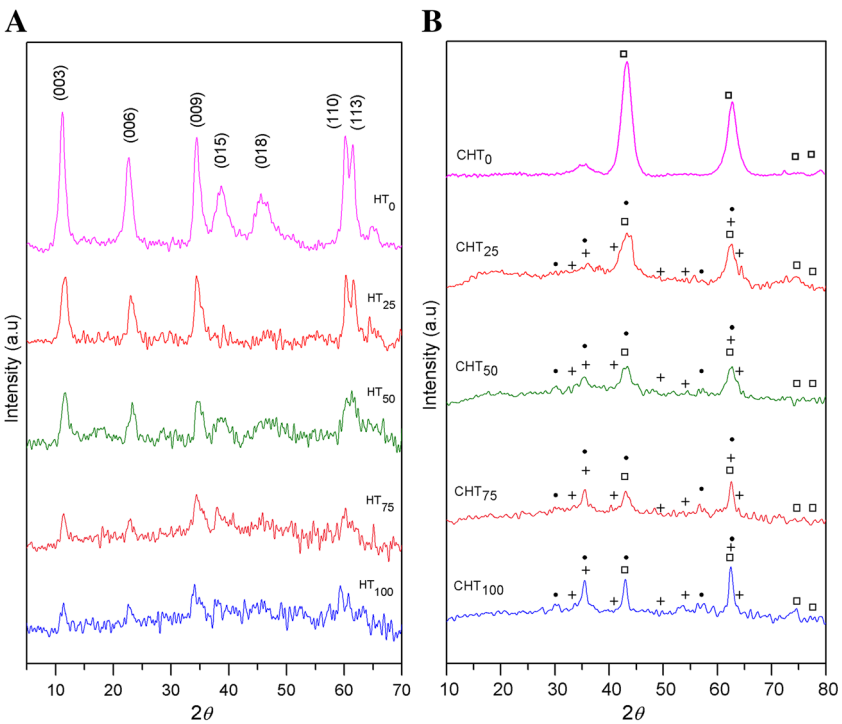

Fig. 1 X-ray diffraction patterns of **a** LDH precursors and **b** calcined samples with different iron content. *Circle* is the spinel $MgFe_2O_4$, *square* is the periclase MgO, and *plus sign* is the hematite Fe_2O_3

a set of bands that can be assigned to the different Fe species [36–39]. In Fig. 2a, all LDH precursors exhibit bands at 207 and 260 nm. Those bands have been assigned to tetrahedral- and octahedral-coordinated Fe^{3+} ions in brucite-layered structure [36]. The band observed at 350 nm has been assigned to small clusters of octahedral Fe^{3+} that would be coordinated to other hydroxides [37]. Therefore, it is expected that octahedral Fe^{3+} remains outside of the lamellar structure in small oxy-hydroxide structures. Finally, the band at 475 nm would correspond to larger iron oxide nanoparticles outside of the lamellar structure [38, 39]. As a consequence, the presence of oxides and hydroxides of Fe^{3+} outside of the lamellar structure is evident when the samples present more than 25% of iron content. Although the size of these oxy-hydroxide iron clusters increases with the content of iron, there is always a fraction of Fe^{3+} ions that keeps tetrahedral and octahedral coordination in the brucite-layered structure [36].

Fig. 2b shows DRUV-Vis spectra of MOs where the bands at 207 and 260 nm, previously assigned to tetrahedral and octahedral coordinated Fe^{3+}, can be also observed. The band at 340 nm has been assigned to isolated Fe^{3+} in periclase Mg(Fe, Al)O and to the spinel $MgFe_2O_4$ [36]. As it was previously indicated, the band at 475 nm could correspond to clusters of iron oxide as well as to relatively large nanoparticles of iron oxide [38–40]. In this regard, the increment on the content of iron would favor not only the presence but also the size of iron nanoparticles in the sample.

Elemental analysis and measurement of SSA and TPV

The amount of the different cations in the samples was determined by ICP spectroscopy of the set of MOs. The values of SSA for partially dehydrated precursors and calcined LDHs samples were determined by the BET method, while the TPVs of calcined samples were estimated by the Barrett-Joyner-Halenda method [41]. The results of elemental analysis, SSA, and TPV experiments are summarized in Table 1.

The ICP analysis of the samples CHT_{75} and CHT_{100} indicates that they have lower content of Mg than the other samples. Besides, it is observed that the values of SSA and TPV diminish with increment of iron concentration. In this regard, the samples HT_0, HT_{25}, and HT_{50} practically duplicate their values of SSA when they are calcined, while the samples with higher iron content present much lower increment of their SSA values. It is well-known that the gradual isomorphous substitutiton of Al^{3+} for Fe^{3+} in the LDH distorts the structure and displaces Mg^{2+} from the brucite layer [42]. Since the ionic radius of Fe^{3+} is bigger than that of Al^{3+}, the structure of LDH is more distorted when the former displaces Mg^{2+}. Consequently, some amount of Mg^{2+} is not incorporated in the LDH structure and the

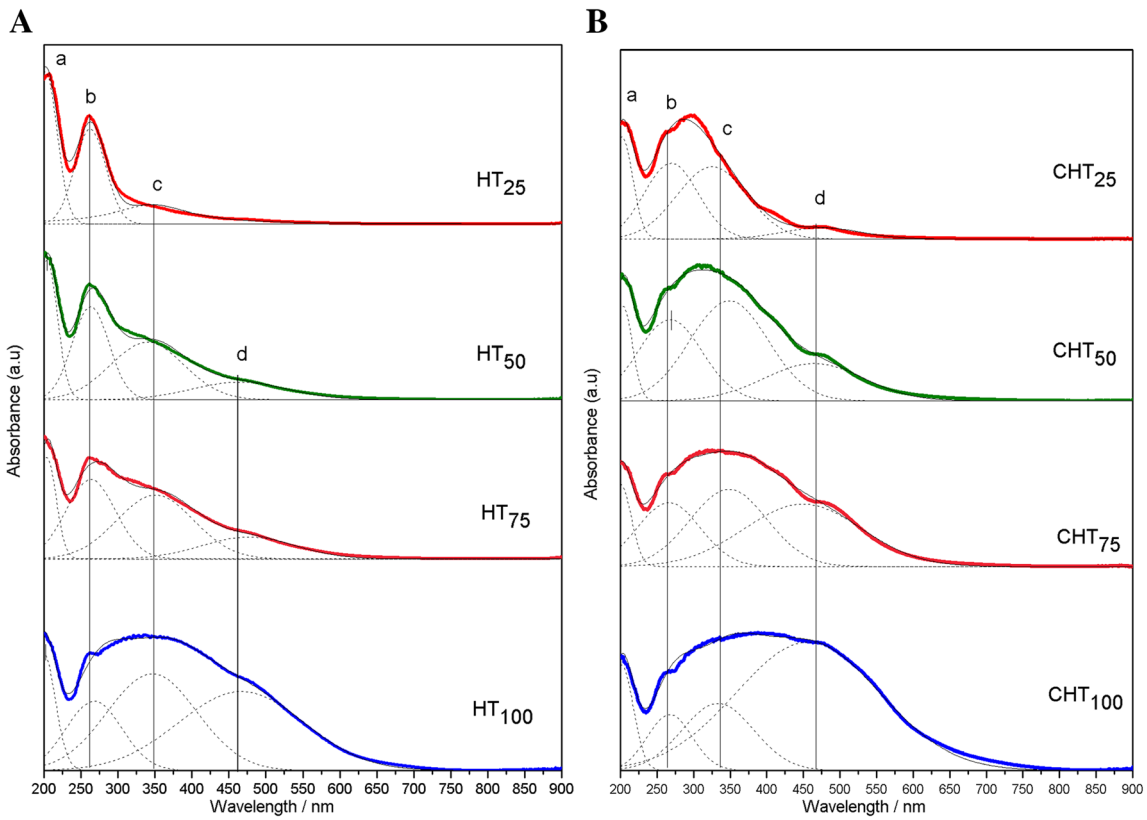

Fig. 2 UV-vis diffuse reflectance spectra. **a** LDH precursors: (*a*) tetrahedral Fe^{3+}, (*b*) octahedral Fe^{3+}, (*c*) octahedral Fe^{3+} in small oxy-hydroxides, and (*d*) Fe^{3+} nanoparticles. **b** Calcined samples: (*a*) tetrahedral Fe^{3+}, (*b*) octahedral Fe^{3+}, (*c*) Fe^{3+} in periclase or spinel phase, and (*d*) Fe^{3+} nanoparticles

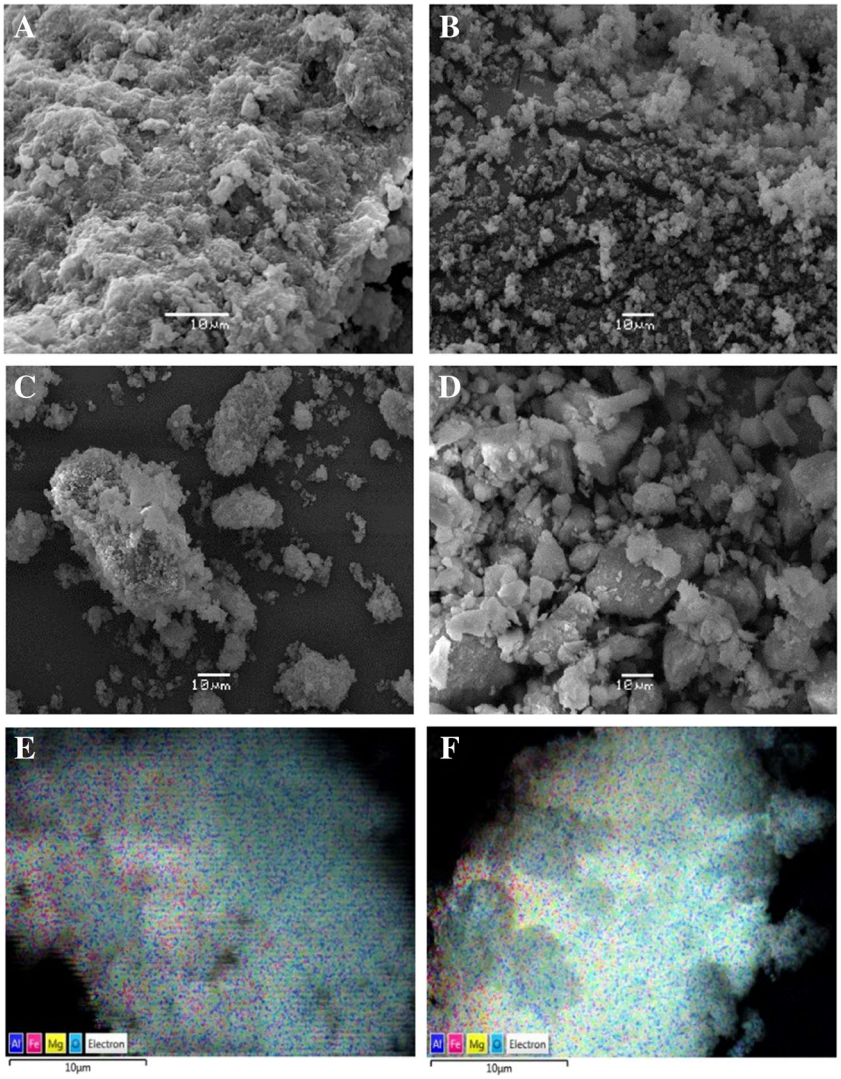

Fig. 3 Micrographs of mixed oxides: **a** CHT_0, **b** CHT_{50}, **c** CHT_{75}, and **d** CHT_{100}. SEM elemental mapping: **e** HT_{25} and **f** CHT_{25}

resulting small grains of HT_{75} and HT_{100} do not significantly change their SSA after being calcined. The MOs have a property denominated the memory effect, which consists of recovering their original LDH structure when they are exposed to an aqueous solution or humid atmosphere.

The structures with low content of aluminum would not be necessarily crystalline, according to the XRD data (Fig. 1). This last fact would indicate that not only the dispersion of the MOs is relatively good but also that sintering effects take place in samples with low content of aluminum. In this regard, relatively large clusters of Fe^{3+} oxides with low or null crystalline structure should be expected for calcined samples with high content of iron. Moreover, the low amount of

Table 2 Molar percentage of metal obtained by mapping SEM analysis

Sample	$\frac{Mg^{2+}\times 100\%}{Mg^{2+}+Al^{3+}+Fe^{3+}}$		$\frac{Al^{3+}\times 100\%}{Mg^{2+}+Al^{3+}+Fe^{3+}}$		$\frac{Fe^{3+}\times 100\%}{Mg^{2+}+Al^{3+}+Fe^{3+}}$	
	Theoretical	Mapping	Theoretical	Mapping	Theoretical	Mapping
CHT_0	75	72.7	25	27.3	0	0
CHT_{25}	75	67.1	18.8	27.1	6.2	5.8
CHT_{50}	75	70.7	12.5	17.6	12.5	11.7
CHT_{100}	75	75.5	0	0	25	24.5

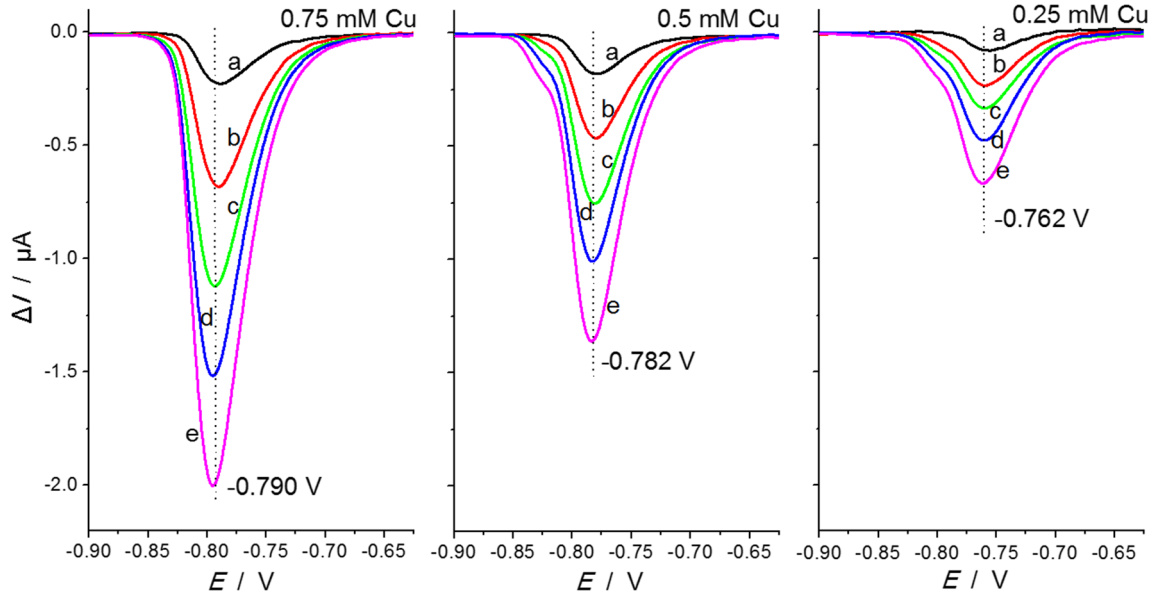

Fig. 4 Response of CS-SWV for solutions with different values of C_{Cu}. f = 100 Hz, E_{sw} = 50 mV, dE = 5 mV, E_{ac} = −0.4 V, t_{ac} = 60 s, E_{ini} = −0.45 V, pH = 0.3, C_{PDTC} = 0.2 μM, and $C_{As(III)}$/μg L^{-1}: (*a*) 10, (*b*) 30, (*c*) 50, (*d*) 70, and (*e*) 100

pores detected for the samples CHT_{75} and CHT_{100} would indicate that the interaction of those particles with the ions of a solution should take place mostly at the surface of the particles.

Study by SEM

Figure 3 shows SEM micrographs of MOs with different iron content. The samples CHT_0 and CHT_{50} exhibit porous structures with small crystalline domains (Fig. 3a, b), while the increment of iron content in the samples induces the formation of smaller and more amorphous structures (Fig. 3c, d). Also, the dispersion of metals has been assessed by elemental maps based on similar SEM micrographs. Figure 3e, f shows images corresponding to the samples HT_{25} and CHT_{25}. Those images resemble the results obtained for the set of samples. As it can be observed, there is good dispersion of metals above the surface before and after calcination. The values of molar percentages corresponding to the different metals at the surface of samples are summarized in Table 2. There is also good

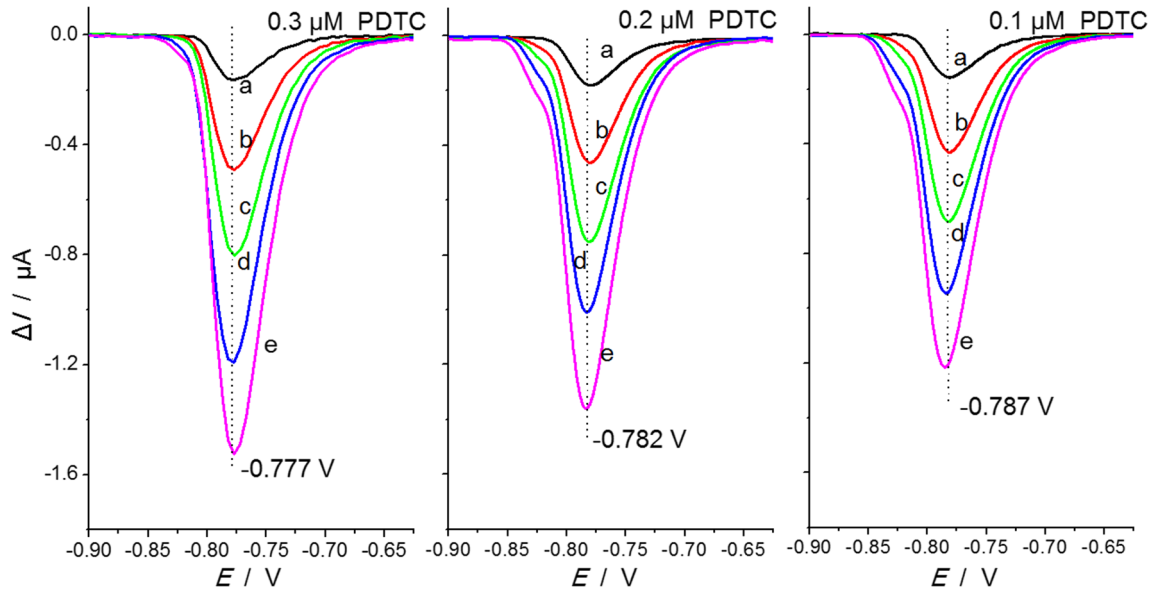

Fig. 5 Response of CS-SWV for solutions with different values of C_{PDTC}. f = 100 Hz, E_{sw} = 50 mV, dE = 5 mV, E_{ac} = −0.4 V, t_{ac} = 60 s, E_{ini} = −0.45 V, pH = 0.3, C_{Cu} = 0.5 mM, and $C_{As(III)}$ /μg L^{-1}: (*a*) 10, (*b*) 30, (*c*) 50, (*d*) 70, and (*e*) 100

correlation between the data expected from the protocol of synthesis and the results corresponding to the elemental mapping.

Effect of PDTC and Cu(II) on the CS-SWV responses of As(III)

It is relatively well-known that the presence of trace amounts of Se and Cu distorts the cathodic response of As due to the formation of intermetallic compounds at the surface of mercury electrodes [30]. However, the use of an excess of Cu(II) contributes not only to minimize the interference of metal cations, including minor amounts of cooper, but also to maximize the electroanalytical response of As(III). Besides, it has been found that trace amounts of arsenic can precipitate with PDTC in presence of Cu(II) ions [43]. Figures 4 and 5 show the differential current (ΔI) of CS-SWV corresponding to samples where the concentrations of Cu(II), PDTC, and As(III) have been varied. As it can be observed from Fig. 4, the presence of Cu(II) clearly contributes to the voltammetric response of arsenic. The peak of ΔI (ΔI_p) is close to −0.8 V and has been assigned to the reduction of As(0) to As(−III) [31, 32]. The value of ΔI_p increases proportionally to the amount of Cu(II) and also changes linearly with $C_{As(III)}$. The voltammetric curves corresponding to 0.25 and 0.5 mM of Cu(II) exhibit the presence of two overlapped processes that might be associated with different intermetallic compounds of Cu and As. Although this problem can be minimized by increasing $C_{Cu(II)}$ to 0.75 mM, it has to be considered that the absolute value of the background current also increases with the concentration of Cu(II). This is because Cu(II) and As(III) are reduced to the species Cu(0) and As(0) at $E = -0.4$ V. Those reduced species interact with PDTC as well as among themselves.

When the potential is close to −0.8 V, during a cathodic scan, the accumulated species of As(0) are reduced to As(−III). The shape of curves points out the presence of an irreversible electrochemical reaction where the reagents are adsorbed at the electrode surface. Moreover, the half-peak width of ΔI is equal to (49 ± 2) mV, indicating that the electrochemical reaction involves the transfer of three electrons [8, 44]. Besides, it has to be considered the effect of one or more chemical reactions coupled to the whole process. In this regard, increment of $C_{Cu(II)}$ shifts the peak potential (E_p) towards more negative values, while the increase of C_{PDTC} shifts the value of E_p in the opposite direction; see Fig. 5. Provided $C_{PDTC} < 0.3$ μM, the addition of PDTC increases the analytical signal and makes it more reproducible. For solutions with higher values of C_{PDTC}, the value of ΔI_p does not change significantly and the drop of Hg is less stable [32].

Figure 6 shows responses of CS-SWV corresponding to the reduction of arsenic at different pH values. As it can be observed, the peak shifts towards more positive potentials and

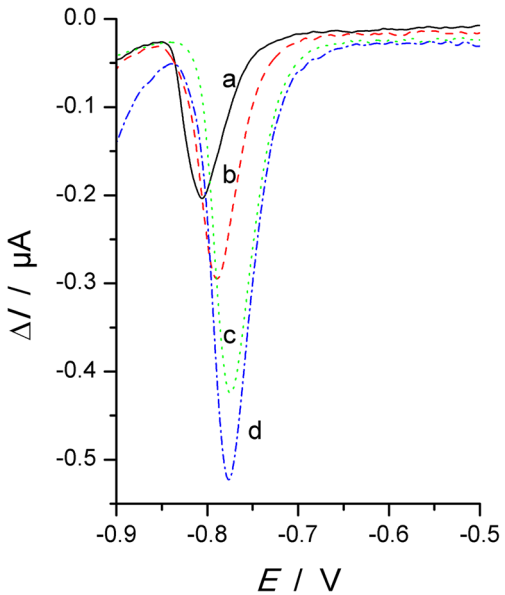

Fig. 6 Response of CS-SWV for solutions with different concentrations of HCl. $f = 100$ Hz, $E_{sw} = 50$ mV, $dE = 5$ mV, $E_{ac} = -0.4$ V, $t_{ac} = 60$ s, $E_{ini} = -0.45$ V, $C_{PDTC} = 0.3$ μM, $C_{Cu} = 0.5$ mM, $C_{As(III)} = 30$ μg L^{-1}, and C_{HCl}/M = (*a*) 0.3 (pH = 0.6), (*b*) 0.6 (pH = 0.4), (*c*) 0.9 (pH = 0.3), and (*d*) 1.2 (pH = 0.1)

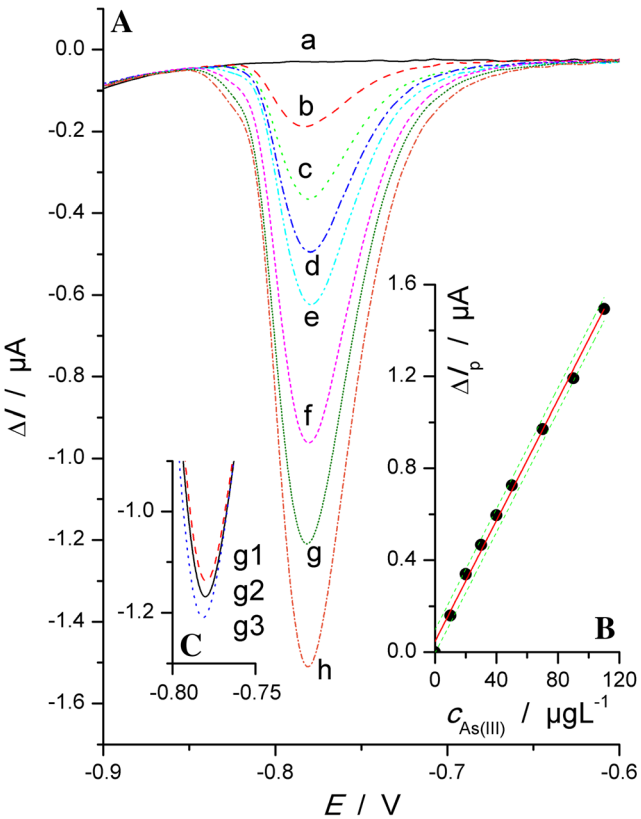

Fig. 7 (*A*) Dependence of CS-SWV on the value of $C_{As(III)}$. (*B*) Dependence of ΔI_p on $C_{As(III)}$. (*C*) Reproducibility of ΔI_p for a solution with value of $C_{As(III)} = 90$ μg L^{-1}. $f = 100$ Hz, $E_{sw} = 50$ mV, $dE = 5$ mV, $E_{ac} = -0.4$ V, $t_{ac} = 60$ s, $E_{ini} = -0.45$ V, pH = 0.3, $C_{PDTC} = 0.3$ μM, and $C_{As(III)}$/μg L^{-1}: (*a*) 0, (*b*) 10, (*c*) 20, (*d*) 30, (*e*) 40, (*f*) 70, (*g*) 90, and (*e*) 110

Table 3 Capacity of MOs for As(III) removal when aliquots of 70 mL at pH = 9.7 are exposed for 10 min to 0.1 g of a MO and then analyzed by CS-SWV using the same parameters of Fig. 7

Samples	Pre-treatment [As]/μg L^{-1}	Post-treatment [As]/μg L^{-1}	Removal %
CHT_0	165.0 ± 0.2	38 ± 2	77
CHT_{50}	165.0 ± 0.2	17 ± 2	90
CHT_{100}	165.0 ± 0.2	20 ± 2	88

the value of ΔI_p increases with the diminution of pH. Furthermore, the background current increases when the solution pH is decreased. The peak corresponding to the solution with C_{HCl} = 0.9 M (pH = 0.3) provides good sensitivity, it is quite symmetric, and it has relatively low background current.

Analytical parameters of CS-SWV measurements

Figure 7 (A) shows SW voltammetric responses for solutions with different $C_{As(III)}$. Curve (a) shows the signal of background electrolyte and the other voltammograms exhibit the dependence of ΔI on the concentration of the analyte. The peak potential is equal to (−0.780 ± 0.003) V and the curves are bell-shaped. The peak of the cathodic current depends linearly on the value of $C_{As(III)}$ (Fig. 7 (B)). The linear behavior ranges from 2 to 110 μg L^{-1}. Above the upper limit, the value of ΔI_p does not change linearly with further additions of arsenic. The reproducibility for the analysis of a sample is better for solutions with low amount of arsenic. In this regard, practically identical voltammetric responses can be obtained for solutions with $2 < C_{As(III)}/\mu g\ L^{-1} < 50$, while the repeatability of signals corresponding to solutions with $C_{As(III)} > 50$ μg L^{-1} would involve an error close to ± 4 μg L^{-1}; see inset of Fig. 7 (C).

According to IUPAC, the value of limit of detection (LOD) can be calculated as three times the ratio between the standard deviation of the blank signal (σ_b) and the slope of the calibration curve [45]. The value of σ_b was determined from the analysis of current values recorded ±30 mV around E_p. Although an excellent value of LOD = 0.2 μg L^{-1} can be obtained in this way, this definition of LOD does not consider the error of the linear regression analysis. Instead, the International Conference on Harmonisation (ICH) suggests the use of three times the standard deviation of the *y*-intercept (σ_y) divided by the slope of the calibration curve (Eq. 3) [46, 47].

$$LOD = 3 \times (0.017\ \mu A)\left(0.013\ \mu A\ \mathrm{L}\ \mu g^{-1}\right)^{-1} \quad (3)$$

This last equation considers the instrumental noise of the signal and the dispersion of data around the linear regression curve [46, 47]. Dashed lines separated by ± 3×σ_y from the linear regression curve are shown in Fig. 7 (B). This method provides a reliable value of LOD = 4 μg L^{-1} that is also consistent with the error observed for measurements with relatively high content of As(III) (Fig. 7 (C)). As a result, the linear range corresponds to $4 \le C_{As(III)}/\mu g\ L^{-1} \le 110$.

As(III) removal by MOs

The capacity of the different calcined samples for As(III) removal was evaluated by CS-SWV. The amount of removed As(III) is expressed as percentage of the ratio between the concentration of As detected before and after exposing a solution of As(III) to a sample of MO. As indicated above, each experiment consisted on exposing an aliquot of 70 mL with 165 μg L^{-1} As(III) to a sample of 0.1 g of MO. This analysis with MOs and arsenic solutions was performed at pH ~ 9.7, which is the natural pH value that results from the synthesis of MOs. Even in those basic solutions, all samples showed significant capacity for removing As(III). The resulting values are expressed as percentage of As(III) removal and summarized in Table 3. Although, competition between arsenide and OH^- anions would be significant at this pH, the samples CHT_{50} and CHT_{100} showed similar and very high capacity for As(III) removal.

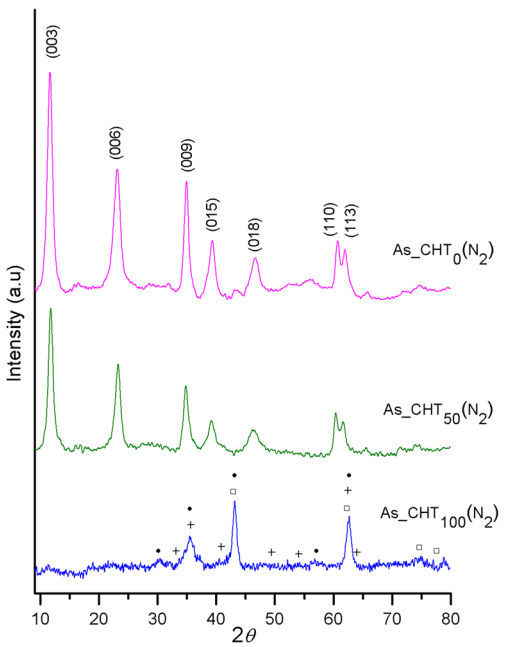

Fig. 8 X-ray diffraction patterns of MOs after As(III) adsorption. Diffraction planes of hydrotalcite-like phases are indicated. *Circle* is the spinel $MgFe_2O_4$, *square* is the periclase MgO, and *plus sign* is the hematite Fe_2O_3

It was expected to observe the highest capacity for removing As(III) with the sample CHT_{100}, since MOs with Fe(III) form more stable complexes with arsenite than with Al(III) [14, 15]. However, the patterns of XRD indicate that the samples As_CHT_0 and As_CHT_{50} can reconstitute the laminar structure of LDHs, while sample As_CHT_{100} would not alter its periclase, spinel, and hematite structures (Fig. 8). This analysis was performed in N_2 atmosphere to prevent the presence of competing species, such as CO_2, that can occupy the interlayer space. Therefore, the interaction of sample As_CHT_{100} with soluble species would take place at the interface of the MOs, whereas the samples As_CHT_0 and As_CHT_{50} can also incorporate arsenite anions within their interlayer spaces.

Although the sample CHT_{50} showed the highest capacity of for removing As(III), it needs to be calcined back to be restored as a filtering material. On the contrary, the sample As_CHT_{100} does not significantly change its structure of MO and it might be restored as the filtering material without a calcination step.

Conclusion

A set of synthetic mixed oxides, feasible of being used as filtering materials, has been characterized by spectroscopic, microscopic, and voltammetric techniques. The MOs were prepared from the coprecipitation of mixtures containing Mg(II), Al(III), and Fe(III), followed by calcination of the layered double hydroxides obtained. The capacity for As(III) removal of the synthesized MOs was studied in a batch reactor using a 10-min contact time. The samples CHT_{50} and CHT_{100} provided an arsenic removal close to 90% when 0.1 g of sample was exposed to 70 mL of 165 μg L^{-1} As(III) solution.

With regard to the structure of synthesized samples, the presence of amorphous Al_2O_3 promotes the dispersion of iron species and increases the surface area. XPS and DRUV-Vis analysis showed that Fe(III) ions can be found in tetrahedral and octahedral coordination environments, while SEM micrographs evidenced the formation of clusters and aggregates of particles according to the increment of the amount of Fe(III) in the solid.

The capacity of MOs for removing As(III) depends on the iron content, surface charge, surface area, and pore volume. The presence of Al(III) contributes to incorporate oxyanions through the pores and to reconstruct the lamellar structure of samples, while Fe(III) favors interactions at the surface of MOs and forms more stable complexes with arsenite. The use of a fraction of Al(III) for the synthesis of MOs provides materials that can incorporate arsenite within the interlayer spaces. Exposition of the samples to carbonated water followed by their calcination at 450 °C can be used to restore the former MO structures.

A protocol for the systematic assessment of samples with arsenite by cathodic stripping square-wave voltammetry has been optimized. The method can be used for determining the concentration of arsenic in samples with 2 μg L^{-1} < [As(III)] < 110 μg L^{-1}. This linear range was suitable for our requirements. Although the LOD value can be lowered by using higher concentration of Cu(II) or longer accumulation times, it is necessary to take in mind that the linear behavior would be confined to two orders of magnitude. This is because the linear range is more related to the standard deviation of the calibration curve than to the error of the baseline.

Acknowledgements Financial support from the Consejo Nacional de Investigaciones Científicas y Tecnológicas (CONICET), Universidad Tecnológica Nacional – Facultad Regional Córdoba (UTN-FRC), Fondo para la Investigación Científica y Tecnológica (FONCYT) PICT-2014-3131, and Secretaría de Ciencia y Tecnología de la Universidad Nacional de Córdoba (SECyT-UNC) is gratefully acknowledged. J. G. A. acknowledges CONICET for the fellowship granted. The authors also wish to thank geol. Julio D. Fernández (UTN-FRC, Córdoba, Argentina) for the help on recording SSA data.

References

1. Hung DQ, Nekrassova O, Compton RG (2004) Talanta 64:269–277
2. Yang M, Guo Z, Li LN, Huang YY, Liu JH, Zhou Q, Chen X, Huang XJ (2016) Sens actuators. B 231:70–78
3. Melamed D (2005) Anal Chim. Acta 532:1–13
4. Fawell JK, Mascarenhas R (2011) Arsenic in drinking-water, Background document for development of WHO Guidelines for Drinking-water Quality.
5. Bathija A (2005) Bromate in drinking-water, Background document for development of WHO Guidelines for Drinking-water Quality
6. Halajnia A, Oustan S, Najafi N, Khataee AR, Lakzian A (2013) Appl Clay Sci 80–81:305–312
7. Ashekuzzaman S, Jiang J (2014) Chem Eng J 246:97–105
8. Robles AD, Vettorelo SN, Gerpe M, Garay F (2017) Electrochim Acta 227:447–454
9. Kameda T, Oba J, Yoshioka T (2016) J Environ Manag 165:280–285
10. Cuéllar M, Vettorelo SN, Ortiz PI, Garay F (2016) J Solid State Electrochem 20:3279–3286
11. Theiss F (2014) F, Couperthwaite S, Ayoko G, Frost RL. J Colloid Interface Sci 417:356–368
12. Ayotte JD, Nolan BT, Nuckols JR, Cantor KP, Robinson GR, Baris D, Hayes L, Karagas M, Bress W, Silverman DT, Lubin JH (2006) Environ Sci Technol 40:3578–3585
13. Forzani ES, Foley K, Westerhoff P, Tao N (2007) Sensors Actuators B Chem 123:82–88
14. Mukherjee P, Chatterjee D, Jana J, Maity PB, Goswami A, Saha H, Sen M, Nath B, Shome D, Joyti Sarkar M, Bagchi D (2007) Household water treatment option: removal of arsenic in presence of natural Fe-containing groundwater by solar oxidation. In: Bhattacharya P, Mukherjee A B, Bundschuh J, Zevenhoven R, Loeppert RH (eds) Trace Metals and other Contaminants in the Environment, vol 9. Elsevier B.V, pp 603–622
15. Hong HJ (2010) Sep Sci Technol 45:1975–1981
16. Mamindy-Pajany Y, Hurel C, Marmier N, Roméo M (2011) Desalination 281:93–99

17. Mohapatra D, Mishra D, Chaudhury GR, Das RP (2007) J Environ Sci Health Part A 42:463–469
18. Hristovski KD, Marcovski J (2017) Sci Total Environ 598:258–271
19. Mayo JT, Yavuz C, Yean S, Cong L, Shipley H, Yu W, Falkner J, Kan A, Tomson M, Colvin VL (2007) Sci Techol Adv Mater 8:71–75
20. Kartinen EO, Martin CJ (1995) Desalination 103:79–88
21. Goh KH, Lim TT, Dong Z (2008) Water Res 42:1343–1368
22. Zhang B, Liu J, Ma X, Zuo P, Ye BC, Li Y (2016) Biosens Bioelectron 80:491–496
23. Feeney R, Kounaves SP (2002) Talanta 58:23–31
24. Toor SK, Devi P, Bansod BKS (2015) Aquat Procedia 4:1107–1113
25. Jia Z, Simm AO, Dai X, Compton RG (2006) J Electroanal Chem 587:247–253
26. Dai X, Nekrassova O, Hyde ME, Compton RG (2004) Anal Chem 76:5924–5929
27. Noskova GN, Zakharova EA, Kolpakova NA, Kabakaev AS (2012) J Solid State Electrochem 16:2459–2472
28. Saha S, Sarkar P (2016) Talanta 158:235–245
29. Gibbon-Walsh K, Salaün P, Van den Berg CMG (2010) Anal Chim Acta 662:1–8
30. Profumo A, Merli D, Pesavento M (2005) Anal Chim Acta 539: 245–250
31. Zima J, Van den Berg CMG (1994) Anal Chim Acta 289:291–298
32. Piech R, Kubiak WW (2007) J Electroanal Chem 599:59–64
33. He Y, Zheng Y, Locke DC (2007) Microchem J 85:265–269
34. The International Centre for Diffraction Data. http://www.icdd.com/. Accessed 08 Jan 2017
35. Cava S, Tebcherani SM, Souza IA, Pianaro SA, Paskocimas CA, Longo E, Varela JA (2007) Mater Chem Phys 103:394–399
36. Heredia AC, Oliva MI, Agú U, Zandalazini CI, Marchetti SG, Herrero ER, Crivello ME (2013) J Magn Magn Mater 342:38–46
37. Centi G, Vazzana F (1999) Catal Today 53:683–693
38. Liu S, Wang Q, Van Der Voort P, Cool P, Vansant E, Jiang M (2004) J Magn Mater 280:31–36
39. Chmielarz L, Kustrowski P, Dziembaj R, Cool P, Vansant E (2006) Appl Catal A 62:369–380
40. Ohishi Y, Kawabata T, Shishido T, Takaki K, Zhang Q, Wang Y, Nomura K, Takehira K (2005) Appl Catal A 288:220–231
41. Liu H, Su D, Wang G, Qiao SZ (2012) Adv Energy Mater 2:970–975
42. Zhang Q, Minami H, Inoue S, Atsuya I (2004) Anal Chim Acta 508:99–105
43. Triantafillidis KS, Peleka EM, Komvokis VG, Mavros PP (2010) J Colloid Interface Sci 342:427–436
44. Mirčeski V, Komorsky-Lovrić S, Lovrić M (2007) Square-wave voltammetry, theory and application. Scholz F (Ed) Monographs in electrochemistry. Springer, berlin
45. Garay F, Kisiel G, Fang A, Lindner E (2010) Anal Bioanal Chem 397:1873–1881
46. Colombo L, Baruzzi AM, Garay F (2015) Sensors Actuators B Chem 211:125–130
47. Shrivastava A, Gupta VB (2011) Chronicle Young Sci 2:21–25